ADVANCED MATERIALS

www.advmat.de

Understanding Detrimental and Beneficial Grain Boundary Effects in Halide Perovskites

*Gede W. P. Adhyaksa, Sarah Brittman, Haralds Āboliņš, Andries Lof, Xueying Li, Joel D. Keelor, Yanqi Luo, Teodor Duevski, Ron M. A. Heeren, Shane R. Ellis, David P. Fenning, and Erik C. Garnett**

Grain boundaries play a key role in the performance of thin-film optoelectronic devices and yet their effect in halide perovskite materials is still not understood. The biggest factor limiting progress is the inability to identify grain boundaries. Noncrystallographic techniques can misidentify grain boundaries, leading to conflicting literature reports about their influence; however, the gold standard – electron backscatter diffraction (EBSD) – destroys halide perovskite thin films. Here, this problem is solved by using a solid-state EBSD detector with 6000 times higher sensitivity than the traditional phosphor screen and camera. Correlating true grain size with photoluminescence lifetime, carrier diffusion length, and mobility shows that grain boundaries are not benign but have a recombination velocity of 1670 cm s^{-1}, comparable to that of crystalline silicon. Amorphous grain boundaries are also observed that give rise to locally brighter photoluminescence intensity and longer lifetimes. This anomalous grain boundary character offers a possible explanation for the mysteriously long lifetime and record efficiency achieved in small grain halide perovskite thin films. It also suggests a new approach for passivating grain boundaries, independent of surface passivation, to lead to even better performance in optoelectronic devices.

Minimizing nonradiative recombination is critical to achieving high efficiencies in optoelectronic devices. Halide perovskites are an emerging class of semiconductors whose optoelectronic properties are tolerant to defects,[1,2] relative to conventional semiconductors. Although the trap density in polycrystalline perovskite films is typically 10^{14}–10^{16} cm^{-3} (as high as 50 per million unit cells),[3,4] their photovoltaic power-conversion efficiencies exceed 20%.[5] Single-crystalline perovskites exhibit far lower trap densities (as low as 10^{10} cm^{-3}),[6] and this difference indicates that polycrystalline thin films possess additional sources of nonradiative recombination such as more bulk defects, less well-passivated surfaces, or grain boundaries.

To improve the efficiency of devices made from polycrystalline perovskites, it is necessary to push the trap density of these films to lower values, toward those reported for single crystals. To achieve this, we first must understand which of these sources of nonradiative recombination is most important to reduce, a task that is complicated by the conflicting reports regarding whether grain boundaries in halide perovskite films are beneficial or detrimental.[7–9] Several studies[10–15] on $CH_3NH_3PbI_3$ perovskite films with grain boundaries less than 5 µm show that carrier lifetime, mobility, and diffusion length increase with grain size, as does the power conversion efficiency of solar cells. These correlations suggest that grain boundaries contribute to nonradiative recombination and reduce device performance. Improvements in performance have also been reported for films with grain size even up to the millimeter scale.[16] In contrast, Kelvin probe force microscopy studies of $CH_3NH_3PbI_3$ films have shown that grain boundaries are beneficial for charge separation and collection,[7] and theory has suggested that PbI_2 at grain boundaries can be beneficial,[17] supporting an earlier hypothesis.[18,19] Furthermore, experiments examining the effects of grains on photovoltaic performance have indicated that heterogeneity of local voltage[20] and crystal facets[21] near grain boundaries are important factors.

All of these studies on perovskite films have inferred the grain size and grain boundary locations based on optical or scanning electron microscopy (SEM) images, which contain no crystallographic information. Therefore, the first step toward understanding the complex effects of grain boundaries is

---

Dr. G. W. P. Adhyaksa, Dr. S. Brittman,[+] H. Āboliņš, A. Lof,
T. Duevski, Prof. E. C. Garnett
Center for Nanophotonics
AMOLF
Science Park 104, 1098 XG, Amsterdam, The Netherlands
E-mail: e.garnett@amolf.nl

X. Li, Y. Luo, Prof. D. P. Fenning
Department of Nanoengineering
University of California San Diego
CA 92093, USA

Dr. J. D. Keelor, Prof. R. M. A. Heeren, Dr. S. R. Ellis
The Maastricht Multimodal Molecular Imaging Institute (M4I)
Division of Imaging Mass Spectrometry
Maastricht University
6229 ER, Maastricht, The Netherlands

The ORCID identification number(s) for the author(s) of this article can be found under https://doi.org/10.1002/adma.201804792.

[+]Present address: U.S. Naval Research Laboratory, 4555 Overlook Avenue SW, Washington, D.C. 20375, USA

DOI: 10.1002/adma.201804792

quantifying their local crystallographic metrics. Traditionally, electron backscatter diffraction (EBSD) is the gold standard for measuring grain size, orientation, and boundary location in thin-film samples. However, its use in halide perovskites has been hampered by beam-induced damage, making EBSD mapping impossible in thin-film samples so far. There has been one report of single spot EBSD measurements, which was limited to single crystals where grain boundaries cannot be studied.[22]

Here, we use a new type of solid-state EBSD detector with 6000 times higher sensitivity than the traditional camera and phosphor screen to collect EBSD maps of grain size and orientation in $CH_3NH_3PbBr_3$ thin films. We developed a thin-film deposition protocol that allows us to control the resulting average grain size over a large range between 1 and 60 µm. We show that the average grain size measured from EBSD is different (up to a factor of ≈1.9) from what is inferred from optical and SEM images. Furthermore, we correlate the accurate values with photoluminescence intensity and lifetime, minority carrier diffusion length, and mobility. Larger grain size (even up to 60 µm) is generally beneficial for all properties. Although most samples show crystalline grain boundaries, samples with amorphous regions at the grain boundaries show properties better than expected according to their grain size. The longer photoluminescence (PL) lifetime and higher PL intensity at these amorphous regions suggest that amorphous interfaces can improve optoelectronic properties, perhaps either by improving grain boundary passivation or gettering native defects. Putting the grain size dependence of optoelectronic properties into a recombination model shows that grain boundary recombination plays an important role in the maximum achievable solar cell and light-emitting diode (LED) efficiency up to grain sizes approaching a millimeter.

In order to systematically study grain boundary effects, we used a deposition procedure that produces continuous and highly oriented films of $CH_3NH_3PbBr_3$.[23] We dissolve $Pb(CH_3COO)_2{\cdot}3H_2O$ and CH_3NH_3Br in dimethylsulfoxide (DMSO) in a 3.05:1 ratio. Changing only the spin-coating time allows us to tune the grain size over a range of 1–60 µm by controlling the nucleation density of an intermediate phase that converts to perovskite upon annealing (details in Supplementary note S1 and Figures S1–S3 in the Supporting Information).[24–27] This method successfully decouples the nucleation and growth steps of the film and therefore offers control over its final grain size on a variety of substrates such as glass, silicon, TiO_2, and indium tin oxide (ITO) (Figure S4, Supporting Information).

We carried out EBSD measurements in an electron microscope that was equipped with a solid-state detector initially designed as a position sensitive, single photon counting detector, from which other applications such as ion and electron detection have evolved (**Figure 1**a).[28,29] The sensor is equipped with an electronic noise free circuit, and therefore provides high sensitivity and fast readout, which enable us to acquire clear EBSD maps of halide perovskite films on glass quickly before damaging the samples. We used an optimized beam current of 100 pA at an accelerating voltage of 30 kV, with a pixel dwell time of 100 ms. The electron dose needed for acquiring EBSD maps here is 6000 times lower than what was previously necessary for single crystal samples using the traditional phosphor screen and camera (6 nA for 10 s).[22] Backscattered electrons escape from the tilted sample and are projected onto the detector in a pattern of spherical bands that reflect the Bragg angles of the local crystal lattice (Kikuchi lines).[30] By scanning the beam across the sample, we collected a pattern from each pixel and indexed it to the cubic $CH_3NH_3PbBr_3$ lattice to construct a map of the film's local crystallographic orientations.

Figure 1b–e shows EBSD maps of the $CH_3NH_3PbBr_3$ perovskite prepared with different spinning times. The grain size becomes larger with reduced spinning time (at a given spin speed), which is consistent with trends inferred from SEM (top panel Figure 1b–e). Most crystal grains are oriented in the [001] direction and the surface orientation propagates throughout the whole film (Figure S10, Supporting Information). On samples with larger than average grain size, however, the population becomes more dispersed to higher index orientations of [101] and [111] because of many smaller crystal grains trapped among adjacent larger grains (bottom panel Figure 1b–e). The mean of the distribution of apparent grain sizes obtained from optical images differs from the mean of the distribution obtained using EBSD (Figure 1g, the method in Figure S5 in the Supporting Information). Typically the difference is less than 40%, but in one particular case (orange trace), the optical images indicate an average grain size of more than a factor of 1.9 larger than the actual grain size. Figure 1f shows the origins of this discrepancy between an SEM image and its corresponding EBSD map. Some pixels of the map show no Kikuchi pattern, for instance, area 4; this indicates a disordered region, which could contain amorphous (not fully crystallized) material,[31] nanocrystalline perovskite with grains much smaller than our interaction volume (≈250 nm based on Monte Carlo simulation; Figure S6, Supporting Information) or a composite of the two. From EBSD data alone, we also cannot rule out the influence of surface roughness (Figure S9, Supporting Information). The observation of disordered regions occurs primarily in the sample with an average grain size of 32 µm. In the optical image, such regions would be incorrectly classified as part of their neighboring grains. Furthermore, the identical Kikuchi patterns between domains 1 and 2 in Figure 1f (across the dashed line) indicate that they are one grain, while their morphology (based on the SEM) suggests there is a grain boundary. In another area (solid line in Figure 1f), the SEM suggests there is no grain boundary but the EBSD map shows that one is present.

To further resolve the origins of the disordered region at the grain boundary, we carried out synchrotron-based nanoprobe X-ray diffraction (nano-XRD) on the sample with <32 µm> grain size (details in Supplementary note S3 and Figure S11 in the Supporting Information). On the basis of the nano-XRD analysis, where no scattering is detected at the grain boundary, the disordered grain boundary regions appear to be amorphous. Figure 1h shows a region of grain boundaries where we detected neither scattering from oriented perovskite [001], nanocrystalline perovskite phase, intermediate phase, nor precursor traces of $PbBr_2$. Our nano-XRD scattering geometry was set to detect [001] scattering, but since other orientations such as [101] or [111] can be easily indexed from the EBSD maps (on smooth surfaces), we believe that the disordered regions at the grain boundaries where we detect neither EBSD nor nanodiffraction intensity are amorphous.

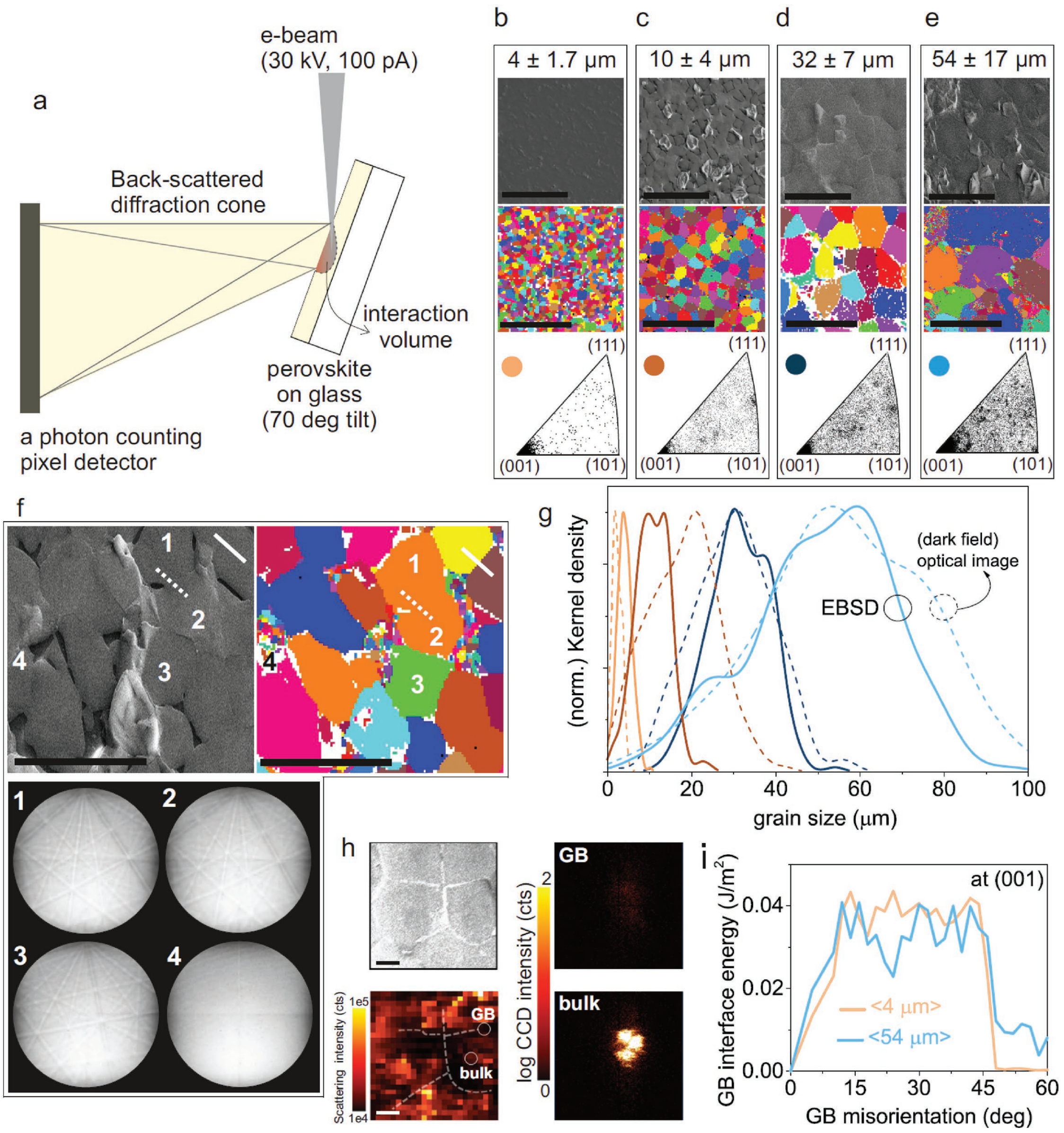

Figure 1. Electron backscattered diffraction (EBSD) maps of CH$_3$NH$_3$PbBr$_3$ perovskite films with different grain sizes. a) Schematic of our EBSD measurement. Collection of scanning electron microscope (SEM) image (top panel) with its corresponding EBSD grain maps (middle panel), and distribution plot of crystallographic orientations (bottom panel) of perovskite films with b) 4 ± 1.7 µm, c) 10 ± 4 µm, d) 32 ± 7 µm, and e) 54 ± 17 µm grain sizes. The EBSD maps for 32 ± 7 µm grain size show disordered regions near the grain boundary (featured as a white color). The color maps do not represent the actual crystallographic orientation. f) Deceiving features of grain boundaries showing two contrasting cases where the boundary that is visible under SEM (top left panel; indicated by the white dashed line) is not an actual grain boundary from the EBSD (see the corresponding EBSD maps; top right panel); whereas within the apparent smooth grain under SEM (top left panel; indicated by the white solid line), there is an invisible grain boundary (top right panel; see the different color maps under the EBSD). The bottom panel shows Kikuchi bands obtained by averaging multiple diffraction patterns per pixel within one scanning area (≈200–600 pixels). The scanning areas 1 and 2 show identical Kikuchi bands, and this pattern is different than that of scanning area 3. Scanning area 4 shows no distinct backscattered diffraction. All scale bars are 50 µm. g) Kernel density distribution of the grain size statistic (with a bandwidth of $h = 0.337$)[78] obtained from the EBSD compared with dark-field optical images. The size of the grains obtained from the optical images can be misleading (by a factor of up to 1.9). h) Top left: SEM image of the grain boundary region. Bottom left: summed scattering intensity across the (002) MAPbBr$_3$ peak when rocking $\theta = 12.86°$, 13.47°, and 14.07° with 2θ fixed at 26.94°. The dashed lines are guides to the eye. Scale bars are 4 µm. Top right: diffraction pattern at the "GB" point highlighted in the scattering intensity map (bottom left). Bottom right: diffraction pattern at the "Bulk" point highlighted in the scattering intensity map. Scale bars are 3 mrad. Neither intermediate nor PbBr$_2$ phases were detected along the grain boundaries (Figure S11, Supporting Information). i) Grain boundary surface energy as a function of grain boundary misorientation for (001) crystal orientation and two grain sizes.

Little is known about the crystallographic nature of grain boundaries in halide perovskites; however, thermodynamically the main characteristics of grain boundaries can be inferred by their crystallographic misorientation angles which can be acquired from the EBSD.[32–35] Using crystallographic misorientation angles, we can calculate the interfacial energy among

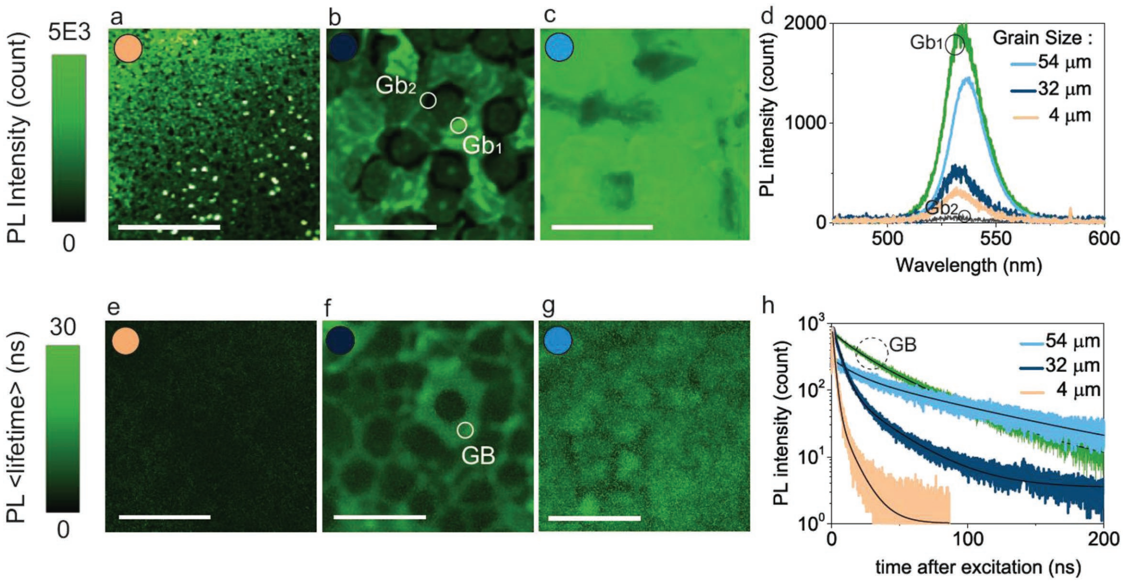

Figure 2. Photoluminescence (PL) intensity and lifetime of $CH_3NH_3PbBr_3$ perovskite films with different grain sizes. PL intensity maps with a) 4 ± 1.7 μm, b) 32 ± 7 μm, and c) 54 ± 17 μm grain sizes, showing that local heterogeneity is more pronounced near the apparent grain boundary for the <32 μm>-grain sample. d) PL spectra showing a similar emission wavelength regardless of the grain sizes; the difference of PL intensity at around the apparent grain boundary for the <32 μm> grain is highlighted (spot Gb1 and spot Gb2). PL effective lifetime maps (integrating time-trace decay that is a convolution of trap-assisted, radiative, and Auger recombination processes) with e) 4 ± 1.7 μm, f) 32 ± 7 μm, and g) 54 ± 17 μm grain sizes. h) Time-resolved PL decay traces showing a faster PL decay for samples with smaller grain sizes. For the sample with medium-sized grains, the PL lifetime near the apparent grain boundary always exhibits a slower decay (spot GB) as compared to its grain interior. The recombination coefficients are extracted by fitting the PL decay traces (black lines). All scale bars (Figure 3a–c,e–g) are 50 μm.

adjacent grain boundaries (details in Supplementary note S2 and Figure S7 in the Supporting Information). For [001] crystal orientation (83% of the $CH_3NH_3PbBr_3$ perovskite film studied here), the grain boundary interfacial energy increases with crystal misorientation angle up to 14°, but then fluctuates without a pronounced global minimum for samples with both the small (<4 μm>) and large (<54 μm>) grain size (Figure 1i). A pronounced global minimum surface energy at high misorientation angle is typically associated with a special boundary, called coherent twinning (e.g., Σ3 or Σ5) which is often observed in other photovoltaic semiconductor materials (CdTe, chalcopyrite, InP, GaAs, and multicrystalline silicon (mc-Si)).[36–40] Removing twinning defects has been shown to improve solar cell performance.[39,40] Although such twinning was previously found on $CsPbX_3$ (X = Cl, Br, I) perovskite nanocrystals,[41] and $CH_3NH_3PbI_3$ thin film,[42] we have not been able to observe it here, even within a smaller spatial resolution of our large-area EBSD mapping (16 nm resolution, 100 nm step size, Figure S9, Supporting Information), or on the higher index crystal orientation [101] and [111]. In mc-Si, for example, the desire to avoid generation of recombination-active intragranular defects such as dislocations and twins has led to a recent trend of reduced grain sizes to improve solar cell performance.[43–49] In contrast, the absence of twinning itself in our films indicates that higher excess interfacial energy at the grain boundary is always induced in order to equilibrate any general structural dislocation (further details of the consequence in Supplementary note S2 and Figure S8 in the Supporting Information).

To understand how the grain boundaries in $CH_3NH_3PbBr_3$ perovskite films affect photogenerated charge carriers, we recorded PL decay profiles on samples each having a different grain size distribution (**Figure 2**). The PL peak was at 534 nm, which is typical for $CH_3NH_3PbBr_3$ perovskite, and the integrated intensity between 475 and 600 nm was used for the lifetime curves. Figure 2 shows that when the PL signal, measured locally, is averaged over the entire map, samples with larger grains yield higher PL intensity and longer lifetimes. In the sample with the largest grains, the apparent grain boundaries appear dark (particularly in the lifetime map), which is consistent with their role as a source of nonradiative recombination and would explain the general trend of longer lifetimes in films with larger grains (further discussion regarding the evolution of recombination coefficients, and the effect of diffusion is in the Supplementary note S4 in the Supporting Information). Unexpectedly, however, the sample with medium-sized grains (Figure 2b) shows PL intensity 30 times brighter and lifetimes 3 times longer at the apparent boundaries as compared to the center of the grain. Using wide-field illumination under a wide range of excitation (10^{16}–10^{18} cm^{-3}) does not alter this increased PL lifetime near the apparent grain boundaries, and therefore indicates that carrier diffusion outside of the collection spot or waveguiding effects are not responsible for this effect (details in Supplementary note S4 and Figures S13 and S14 in the Supporting Information).[13,50,51] Furthermore, by analyzing the local PL intensity as a function of carrier density both near the apparent boundaries and in the center of grains, we confirmed that local variations in doping are also not responsible for the difference in PL intensity (Supplementary note S4, subsection local doping effect and Figure S15, Supporting Information). EBSD maps together with nano-XRD analysis indicate that these grain boundaries consist of an amorphous phase (Figure 1h). Secondary ion mass spectroscopy (SIMS) maps taken with 192 nm pixel size and X-ray photoelectron spectroscopy (XPS) analysis suggest that the bulk and surface composition of the sample with amorphous boundaries do not differ compared to the other samples with crystalline boundaries. There are some local compositional variations that are similar across all films, but these variations do not correlate with the spatial variations in the PL lifetime or intensity (details in Supplementary notes S7 and S8, Figures S19 and S20 in the Supporting Information). Interestingly, the qualitatively different nature of such an amorphous phase at grain boundaries could explain the mysteriously long lifetimes, large local variations, and excellent efficiency seen in some small grain halide perovskite thin-film devices. Furthermore, known chemical passivation treatments might also be creating amorphous regions or surface layers that could account for some of their effectiveness.[8,72] Our measurements show that the amorphous phase has higher PL intensity and lifetime than the bulk perovskite; however, the longer lifetime does not necessarily indicate improved photovoltaic performance, which depends on the charge carrier diffusion length that is a function of both carrier lifetime and mobility.[52]

To understand the role of grain boundaries in halide perovskites on electronic transport, we used the steady-state photocarrier grating (SSPG) technique to measure the ambipolar charge-carrier diffusion length within the films.[12,53] This technique relies on measuring lateral carrier transport in the film in the presence of sinusoidal laser interference (an optical grating) created by two monochromatic lasers (450 nm excitation wavelength) where one laser is weaker than the other. Any carrier diffusion length longer than the interference periodicity will smear out the grating's amplitude, and therefore the sample's conductivity can be measured. By monitoring how the sample's conductivity changes as a function of the period of the grating, the minority carrier diffusion length can be extracted (details in Supplementary note S5 in the Supporting Information).[54,55] Using a similar laser excitation wavelength for the SSPG and PL measurements (480 nm), we expect the distribution of the photogenerated carriers to be similar, given that all the films have similar background carrier concentration (Supplementary note S5 and Figure S18, Supporting Information). We carried out the measurement on the same samples used earlier for the PL studies and observed that the minority carrier diffusion length increases with grain size (Figure S17, Supporting Information). The diffusion lengths extracted range from 168 to 548 nm with increasing grain size from <4 µm> to <54 µm>. These data clearly show that the increased grain size still improves the lateral carrier transport, even if the grain size is two orders of magnitude larger than the diffusion length.

Generally, we observed that $CH_3NH_3PbBr_3$ perovskite films with larger grains yield longer PL lifetimes; however, PL lifetimes for the <32 µm> grained film were longer than expected (Figure 2 and Figure S13 (Supporting Information) at variable excitation intensity). For each sample, we collected ≈20 maps of PL lifetime, each from a different spot, and tabulated the trap-assisted (monomolecular) lifetime as a function of grain size in **Figure 3**a. Each data point represents an ≈80 × 80 µm^2 PL lifetime map. We find that the mean PL lifetime (see the distribution on the right y-axis, Figure 3a) of the <32 µm>-grain sample is longer than that of the <54 µm>-grain sample,

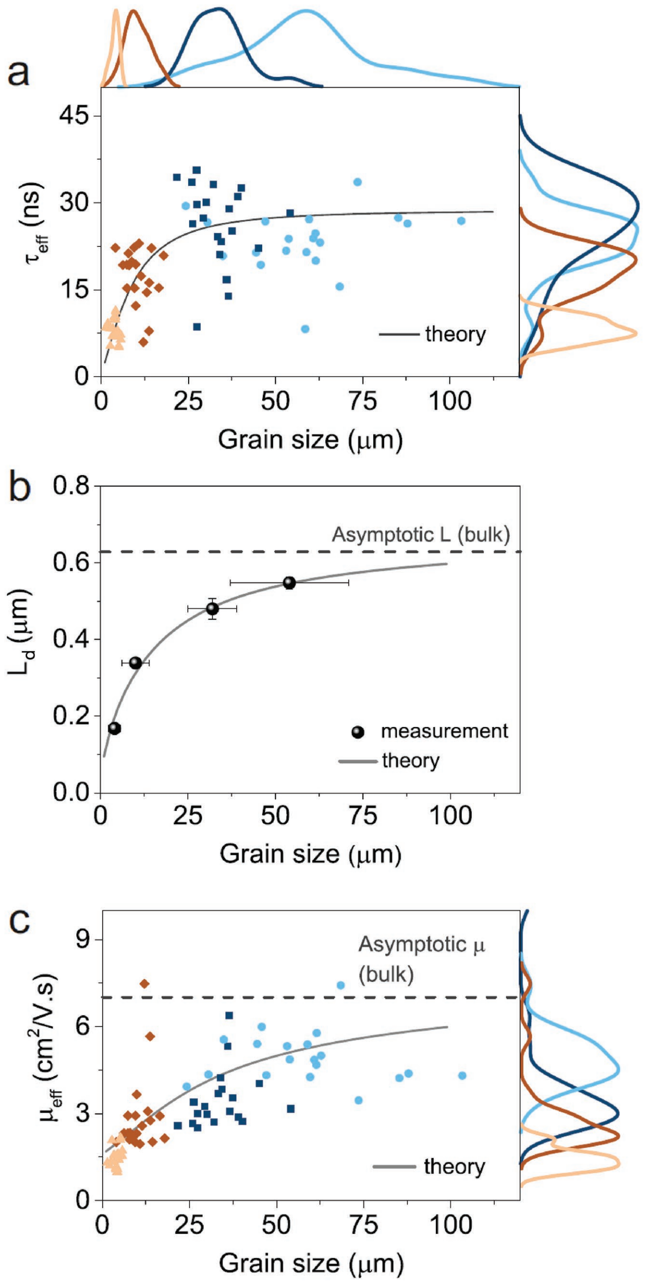

Figure 3. Statistical correlation of grain sizes and optoelectronic properties of $CH_3NH_3PbBr_3$ perovskite. a) The effective carrier lifetimes (τ_{eff}) versus grain sizes. The τ_{eff} is extracted from the PL decay traces where each point represents an area mapping of 80 µm × 80 µm size within the same substrate; right y-axis: the kernel distribution (with a bandwidth of $h = 0.337$)[78] is to illustrate the distributions of the extracted τ_{eff}; top x-axis: distributions of grain sizes from EBSD (identical to Figure 1g). b) Minority carrier diffusion length (L_d) versus grain size; the L_d values are extracted from steady-state photocarrier grating measurements (SSPG) across scanning areas of ≈0.5 cm × 0.5 cm; the y-error bars represent linear propagation of error from the measurement, while x-error bars represent a 95% confidence interval. c) Carrier mobility (μ_{eff}) versus grain size; the data are calculated from each data point of τ_{eff} (a) and the L_d values (b). All measurements were conducted on identical samples with nearly the same spot area.

even under wide-field illumination (Figure S14, Supporting Information), which suggests that the grain boundaries in the <32 µm> sample have a different electronic character than those in the other samples. This special electronic character is consistent with the amorphous nature of the grain boundary. Figure 3b shows that the diffusion length increases with grain size. The absence of the anomaly at <32 µm>-grain sample suggests that the increase in PL lifetime is coupled to a decrease in carrier mobility.

To quantify this relationship, we used Fourier decomposition to solve the steady-state diffusion equation and fit this analytical solution to the data (details in Supplementary note S6 in the Supporting Information). We modeled and fit the data numerically; however to obtain an intuitive picture, we can approximate the dependence of carrier diffusion length on grain size by examining the first term in a truncated Fourier expansion.[56–64]

$$L_{\mathrm{d}} = \left(\frac{2S_{\mathrm{GB}}}{DG} + \frac{1}{(LA)^2} \right)^{-1/2} \tag{1}$$

where L_{d} is the minority carrier diffusion length (value that is obtained from the SSPG measurement), S_{GB} is the grain boundary recombination velocity, D is the asymptotic value of the diffusion coefficient of the polycrystalline thin film, G is the grain size, L is the asymptotic value of the diffusion length of the polycrystalline thin film, and A is defined as

$$A = \frac{1 + \dfrac{S_{\mathrm{FB}}L}{D} \tanh\left(\dfrac{W}{L}\right)}{\dfrac{S_{\mathrm{FB}}L}{D} + \tanh\left(\dfrac{W}{L}\right)} \tag{2}$$

where S_{FB} is the front or back surface recombination velocity (assumed to be the same), and W the is film thickness. G, L, D, L_{d}, and W are known from the experiments, whereas S_{GB} and S_{FB} were used as free fitting parameters. The values of L and D depend on the quality of the bulk perovskite material and are the asymptotic values of the experimental data for L_{d} and D calculated using the Einstein relation and the asymptotic effective mobility (μ_{eff}) at which the effect of grain boundaries is no longer relevant (Figure 3b,c). After global optimization, we find that the solutions for S_{GB}, S_{FB}, L, and D in our sample are 1670 ± 50 cm s^{-1}, 27 ± 1.5 cm s^{-1}, 0.61 µm, and 0.18 cm^2 s^{-1}, respectively. Note that with a surface recombination velocity (S_{FB}) 30 times lower than the grain boundary recombination velocity (S_{GB}), grain boundaries still play a significant role in transport up to a grain size of ≈20 µm (≈35% contribution to L_{d}). For larger grains, the surface recombination then becomes more influential. Grain boundary recombination accounts for 80% of the reduced L_{d} when the ratio W/L is 1 (perovskite thickness of 610 nm); much smaller values for W/L (less than ≈0.01) are needed before surface recombination dominates. The grain boundary recombination velocity in our polycrystalline $CH_3NH_3PbBr_3$ film is comparable to the surface recombination velocity of single crystalline $CH_3NH_3PbBr_3$ reported by Yang et al.[65] The recombination velocity at the grain boundary for a halide perovskite has not been reported before, but the values obtained here fall around an order of magnitude higher than that of unpassivated CdTe[66] and similar to passivated mc-Si[67,68] or copper indium gallium selenide (CIGS).[69,70]

We can calculate an effective mobility indirectly from the diffusion length measurement (Figure 3b) and the PL lifetime data (Figure 3a). We find that except for the <32 µm>-grain sample, the effective mobility increases with grain size (Figure 3c); a similar trend was previously reported for $CH_3NH_3PbI_3$ films.[10] In the <32 µm>-grain sample, the amorphous grain boundaries appear to limit mobility because this sample's diffusion length is unchanged, while its lifetimes are anomalously long. The mobility in our $CH_3NH_3PbBr_3$ samples ranges between ≈1.5 and 7.5 cm^2 V^{-1} s^{-1}, similar to the values estimated from PL quenching measurements.[71] The effective mobility presented here is the intrinsic ambipolar transport mobility which will be dominated by the excess carrier with shorter diffusion length (details in Supplementary note S5 and Table S2 in the Supporting Information), thus isolating any effect from transporting layers.

Understanding the role of grain boundaries in perovskite solar cells is essential to push these devices to their peak performance. As a first approximation, grain boundary effects in halide perovskite films have been neglected when the grain size is much larger than the film thickness[16] and all grain boundaries have been treated as having the same effect on performance. In halide perovskite films with grain sizes comparable to the film thickness (less than 1 µm), some studies have reported that grain boundaries reduce mobility,[10] diffusion length,[12] and solar cell performance,[11] but they did not use a crystallographic technique to measure grain size. Such work led to more recent attempts to passivate surfaces and grain boundaries to improve device performance.[72–74] Until now, grain boundary passivation studies have focused on chemical passivation, but without studying the crystallographic nature of the grain boundaries, it is not possible to exclude crystallographic rather than chemical effects. In fact, our study showing highly disordered (likely amorphous) material at some grain boundaries with anomalously high PL intensity and lifetime suggests that chemical passivation may not be the only contributing factor. It is therefore valuable to revisit current chemical grain boundary passivation studies to see if there are any crystallographic changes in the films induced by the use of additives intended for passivation.

Here, we provide a more detailed view of grain boundaries. We have shown in a $CH_3NH_3PbBr_3$ system made from a lead-acetate precursor that grain boundaries still play a dominant role in the optoelectronic properties up to the range of <20 µm>, after which surface recombination dominates. We also show that crystalline grain boundaries behave qualitatively differently than those containing amorphous perovskite. The relatively high surface recombination velocity of $CH_3NH_3PbI_3$ (450 cm s^{-1})[75] compared to our films (27 cm s^{-1}) suggests that grain boundaries will become a major source of losses in record solar cells once improvements in $CH_3NH_3PbI_3$ surface passivation are made.

To examine such effects, we model a solar cell and compute the maximum attainable photoluminescence quantum yield (PLQY) based on our film's characteristics ($S_{\mathrm{GB}} = 1670$ cm s^{-1}, $S_{\mathrm{FB}} = 27$ cm s^{-1}, $L = 0.61$ µm, and $D = 0.18$ cm^2 s^{-1}, details in Supplementary note S6 in the Supporting Information). The

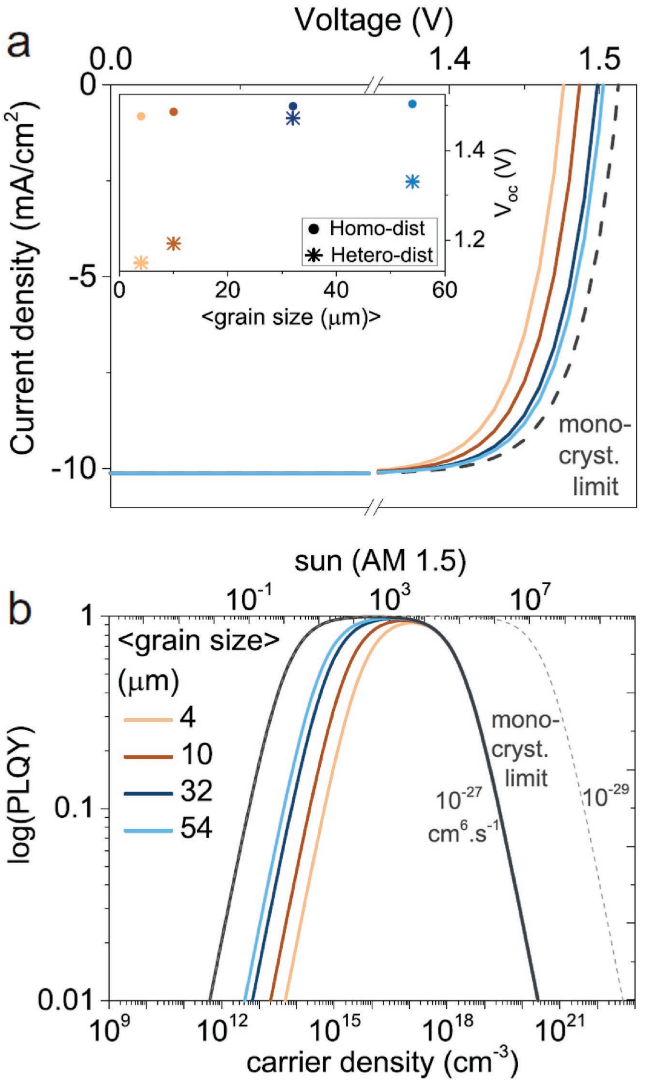

Figure 4. Modeling the characteristics of solar cells and photoluminescence quantum yield with different grain sizes of $CH_3NH_3PbBr_3$ perovskite. a) Simulated *I–V* curve showing that larger grain size increases V_{oc}. This correlation becomes randomized when the heterogeneity of grain size (the experimental standard deviation) is introduced into the model (the inset). Colors have the same labels in both panels. b) Simulated PLQY as a function of the carrier density for different grain sizes using experimentally determined parameters; the PLQY at higher fluence is mainly limited by Auger recombination with two limiting values chosen from the literature.[79,80]

solar cell consists of a planar polycrystalline $CH_3NH_3PbBr_3$ absorber layer sandwiched between two transporting layers (TiO_2, and NiO_x) and metal contacts (fluorine-doped tin oxide (FTO), and Au). Carrier transport is assumed to be isotropic; however, given recent reports on rapid carrier diffusion within grains,[8,51] carrier transport within a perovskite thin film might be more accurately modeled anisotropically and therefore, our results can be considered an upper bound for the detrimental influence of grain boundaries. **Figure 4**a shows simulated *J–V* curves of solar cells with different grain sizes (homogeneous grain size for each). The grain size primarily regulates the open-circuit voltage (V_{oc}), with minimal impact on the short-circuit current density (J_{sc}). If we assume a grain size distribution (as observed experimentally), then there is significant heterogeneity of the simulated local voltage of each individual grain. Since the full device can be modeled as a collection of individual grains connected electrically in parallel, the V_{oc} is limited by the smallest grains in this distribution.[76] For example, when the width of the distribution is ≈30% of the average grain size, the V_{oc} drops from ≈1.5 to ≈1.33 V, precluding simple experimental device studies of the effect of grain size because samples with larger grain sizes also have wider distributions (inset in Figure 4a). Both the average and the distribution must be taken into account. This heterogeneity effect, however, is almost negligible if the device is stacked laterally, resembling an interdigitated back contact solar cell.[77] In this regard, moving toward monocrystalline thin films for solar cells is still necessary for better device performance: completely removing grain boundaries from a 4 µm grain size halide perovskite film would increase V_{oc} by 110 mV (8%) in a solar cell with ideal contacts (67 mV increase in V_{oc} with simulated contact losses, Figure 4a). Clearly, minimizing the effects of grain boundaries is still required to improve the device performance.

Next, we simulated the PLQY of our films by assuming that all losses at the grain boundary, on the front/back surface, and in the bulk contribute to monomolecular trap-assisted recombination. The analytical expression of Equations (1) and (2) can be used to convert the minority carrier diffusion length into an effective lifetime that is inversely proportional to monomolecular recombination coefficient as a function of grain size (details in Supplementary note S6 in the Supporting Information). The carrier density required to reach a PLQY of 1% is reduced by one order of magnitude when we increase the grain size from 4 to 54 µm, and by two orders of magnitude when all grain boundaries are removed (monocrystalline film, Figure 4b). Having relatively large grain sizes up to 54 µm is still not enough to reach the monocrystalline total integrated PLQY. We estimate that a half-millimeter grain size is required to get 96% of the monocrystalline performance, which is particularly important for 1 sun applications.

In conclusion, here we show the importance of using a true crystallographic measurement when studying the effect of grain boundaries in halide perovskite thin films. This is not only necessary for proper identification of grain boundaries but also enables deeper insights from studying dependence on misorientation angle, disorder at the interface, and heterogeneity in grain size. Using EBSD, we find that twinning does not play a role in the $CH_3NH_3PbBr_3$ films studied here, but the grain boundary recombination velocity of 1670 ± 50 cm s^{-1} plays a key role in lowering performance. Our modeling suggests that increasing the average grain size (and uniformity) to close to a millimeter or drastically lowering grain boundary recombination velocity is necessary to approach the limiting efficiency potential. Interestingly, under certain conditions, amorphous regions can form at the grain boundaries, increasing photoluminescence intensity and lifetime without degrading carrier diffusion length. These results might explain the conflicting literature reports of grain boundary effects in halide perovskites: crystalline grain boundaries are detrimental to performance, while amorphous regions can provide excellent passivation and longer lifetimes.

Supporting Information

Supporting Information is available from the Wiley Online Library or from the author.

Acknowledgements

The authors thank Dr. Bruno Ehrler and Dr. Aditya Mohite for giving feedback on the paper. E.C.G., A.L., and G.W.P.A. thank Hans Poolman, Dmytro Byelov, Erik Maddox, and Dirk-Jan Spaanderman for fruitful discussions and support regarding the EBSD detector. G.W.P.A. thanks Luc Blom, Jan Zomerdijk, Erik Clay, Marnix Verweij, and Marc Duursma for their support in developing the SSPG setup, Dr. Sophie Meuret for helpful discussion on electron beam interactions with solids, Reinout Jaarsma and Johannes Kirschner for assistance with XPS measurements, Benjamin Daiber and Stefan Tabernig for help during the wide-field PL experiment, and Indra Sihar for helpful discussion on finite element analysis. S.B. and T.D. thank Dr. Forrest Bradbury for helpful discussions about the PL lifetime fitting routine. D.P.F., X.L., and Y.L. thank Martin Holt and Zhonghou Cai for supporting the nanodiffraction measurements, Shen Wang for assistance with focused ion beam (FIB) marker preparation, and the Hellman Foundation and the California Energy Commission (Grant No. EPC-16-050) for financial support. Use of the Center for Nanoscale Materials and the Advanced Photon Source, both Office of Science user facilities, was supported by the U.S. Department of Energy, Office of Science, Office of Basic Energy Sciences, under Contract No. DE-AC02-06CH11357. G.W.P.A. was supported by the TKI Urban Energy, "COMPASS" (TEID215022), at the end of this project. This work is part of The Netherlands Organization for Scientific Research (NWO). The work performed by the Maastricht University was supported by the Dutch province of Limburg through the LINK programme. The authors acknowledge financial support from the European Research Council under the European Union's Seventh Framework Programme (Grant No. FP/2007- 2013)/ERC Grant Agreement No. 337328, "NanoEnabledPV," and from an industrial partnership between Philips and FOM.

E.C.G. and S.B. conceived the idea. G.W.P.A. wrote the paper under the supervision of E.C.G., S.B., and D.P.F. H.A. and S.B. developed the controlled grain size deposition protocol. A.L. and G.W.P.A. carried out the electron backscattered diffraction measurements and analysis. X.L. and Y.L. carried out the synchrotron-based nanoprobe X-ray diffraction and analysis under the supervision of D.P.F. J.D.K. carried out time-of-flight (TOF)-secondary ion mass spectrometry (SIMS) measurement and analysis under the supervision of S.R.E. (the latter with S.B.). T.D. developed the photoluminescence lifetime fitting routine with S.B. G.W.P.A. and S.B. designed and analyzed the photoluminescence experiments, and G.W.P.A. conducted the photoluminescence and diffusion length measurements, developed the theoretical modeling, and built the steady-state photocarrier grating setup under the supervision of E.C.G. All authors discussed the results and reviewed the final paper.

Conflict of Interest

The EBSD detector used in this study is now being commercialized by Amsterdam Scientific Instruments.

Keywords

amorphous grain boundaries, carrier lifetime, diffusion length, electron backscatter diffraction (EBSD), grain size effect, halide perovskites, mobility

Received: July 26, 2018
Revised: September 25, 2018

[1] W.-J. Yin, T. Shi, Y. Yan, *Appl. Phys. Lett.* **2014**, *104*, 063903.
[2] A. Walsh, D. O. Scanlon, S. Chen, X. G. Gong, S.-H. Wei, *Angew. Chem., Int. Ed.* **2015**, *54*, 1791.
[3] S. Heo, G. Seo, Y. Lee, D. Lee, M. Seol, J. Lee, J.-B. Park, K. Kim, D.-J. Yun, Y. S. Kim, J. K. Shin, T. K. Ahn, M. K. Nazeeruddin, *Energy Environ. Sci.* **2017**, *10*, 1128.
[4] G. Xing, N. Mathews, S. S. Lim, N. Yantara, X. Liu, D. Sabba, M. Grätzel, S. Mhaisalkar, T. C. Sum, *Nat. Mater.* **2014**, *13*, 476.
[5] S. D. Stranks, *ACS Energy Lett.* **2017**, *2*, 1515.
[6] D. Shi, V. Adinolfi, R. Comin, M. Yuan, E. Alarousu, A. Buin, Y. Chen, S. Hoogland, A. Rothenberger, K. Katsiev, Y. Losovyj, X. Zhang, P. A. Dowben, O. F. Mohammed, E. H. Sargent, O. M. Bakr, *Science* **2015**, *347*, 519.
[7] J. S. Yun, A. Ho-Baillie, S. Huang, S. H. Woo, Y. Heo, J. Seidel, F. Huang, Y.-B. Cheng, M. A. Green, *J. Phys. Chem. Lett.* **2015**, *6*, 875.
[8] D. W. de Quilettes, S. M. Vorpahl, S. D. Stranks, H. Nagaoka, G. E. Eperon, M. E. Ziffer, H. J. Snaith, D. S. Ginger, *Science* **2015**, *348*, 683.
[9] D.-Y. Son, J.-W. Lee, Y. J. Choi, I.-H. Jang, S. Lee, P. J. Yoo, H. Shin, N. Ahn, M. Choi, D. Kim, N.-G. Park, *Nat. Energy* **2016**, *1*, 8.
[10] O. G. Reid, M. Yang, N. Kopidakis, K. Zhu, G. Rumbles, *ACS Energy Lett.* **2016**, *1*, 561.
[11] H. D. Kim, H. Ohkita, H. Benten, S. Ito, *Adv. Mater.* **2016**, *28*, 917.
[12] G. W. P. Adhyaksa, L. W. Veldhuizen, Y. Kuang, S. Brittman, R. E. I. Schropp, E. C. Garnett, *Chem. Mater.* **2016**, *28*, 5259.
[13] M. Yang, Y. Zeng, Z. Li, D. Hoe Kim, C.-S. Jiang, J. van de Lagemaat, K. Zhu, *Phys. Chem. Chem. Phys.* **2017**, *19*, 5043.
[14] D. Fisher, F. Saouma, J. Jang, T. P. Dhakal, in *IEEE 43rd Photovoltaic Specialists Conf. (PVSC)*, IEEE, Piscataway, NJ, USA **2016**, pp. 0768-0772.
[15] X. Ren, Z. Yang, D. Yang, X. Zhang, D. Cui, Y. Liu, Q. Wei, H. Fana, S. F. Liu, *Nanoscale* **2016**, *8*, 3816.
[16] W. Nie, H. Tsai, R. Asadpour, J.-C. Blancon, A. J. Neukirch, G. Gupta, J. J. Crochet, M. Chhowalla, S. Tretiak, M. A. Alam, H.-L. Wang, A. D. Mohite, *Science* **2015**, *347*, 522.
[17] J. Haruyama, K. Sodeyama, L. Han, Y. Tateyama, *J. Phys. Chem. Lett.* **2014**, *16*, 2903.
[18] T. Jesper Jacobsson, J.-P. Correa-Baena, E. H. Anaraki, B. Philippe, S. D. Stranks, M. E. F. Bouduban, W. Tress, K. Schenk, J. Teuscher, J.-E. Moser, H. Rensmo, A. Hagfeldt, *J. Am. Chem. Soc.* **2016**, *138*, 10331.
[19] Q. Chen, H. Zhou, T.-B. Song, S. Luo, Z. Hong, H.-S. Duan, L. Dou, Y. Liu, Y. Yang, *Nano Lett.* **2014**, *14*, 4158.
[20] G. E. Eperon, D. Moerman, D. S. Ginger, *ACS Nano* **2016**, *10*, 10258.
[21] S. Y. Leblebici, L. Leppert, Y. Li, S. E. Reyes-Lillo, S. Wickenburg, E. Wong, J. Lee, M. Melli, D. Ziegler, D. K. Angell, D. F. Ogletree, P. D. Ashby, F. M. Toma, J. B. Neaton, I. D. Sharp, A. Weber-Bargioni, *Nat. Energy* **2016**, *1*, 16093.
[22] P. Khoram, S. Brittman, W. I. Dzik, J. N. H. Reek, E. C. Garnett, *J. Phys. Chem. C* **2016**, *120*, 6475.
[23] N. Giesbrecht, J. Schlipf, L. Oesinghaus, A. Binek, T. Bein, P. Müller-Buschbaum, P. Docampo, *ACS Energy Lett.* **2016**, *1*, 150.
[24] N. J. Jeon, J. H. Noh, Y. C. Kim, W. S. Yang, S. Ryu, S. I. Seok, *Nat. Mater.* **2014**, *13*, 897.
[25] J. S. Manser, M. I. Saidaminov, J. A. Christians, O. M. Bakr, P. V. Kamat, *Acc. Chem. Res.* **2016**, *49*, 330.
[26] Y. Guo, K. Shoyama, W. Sato, Y. Matsuo, K. Inoue, K. Harano, C. Liu, H. Tanaka, E. Nakamura, *J. Am. Chem. Soc.* **2015**, *137*, 15907.
[27] Y. Rong, S. Venkatesan, R. Guo, Y. Wang, J. Bao, W. Li, Z. Fan, Y. Yao, *Nanoscale* **2016**, *8*, 12892.
[28] J. Visser, B. van der Heijden, S. J. A. Weijers, R. de Vries, J. L. Visschers, *Nucl. Instrum. Methods Phys. Res., Sect. A* **2011**, *633*, S22.

[29] X. Llopart, R. Ballabriga, M. Campbell, L. Tlustos, W. Wong, *Nucl. Instrum. Methods Phys. Res., Sect. A* **2007**, *581*, 485.
[30] E. Levine, W. L. Bell, G. Thomas, *J. Appl. Phys.* **1966**, *37*, 2141.
[31] J. J. Choi, X. Yang, Z. M. Norman, S. J. L. Billinge, J. S. Owen, *Nano Lett.* **2014**, *14*, 127.
[32] B. L. Adams, S. Ta'Asan, D. Kinderlehrer, I. Livshits, D. E. Mason, C.-T. Wu, W. W. Mullins, G. S. Rohrer, A. D. Rollett, D. M. Saylor, *Interface Sci.* **1999**, *7*, 321.
[33] W. T. Read, W. Shockley, *Phys. Rev.* **1950**, *78*, 275.
[34] Y. Huang, F. J. Humphreys, *Acta Mater.* **1999**, *47*, 2259.
[35] M. Taheri, H. Weiland, A. Rollett, *Metall. Mater. Trans. A* **2006**, *37*, 19.
[36] D. Abou-Ras, K. Pantleon, *Phys. Status Solidi RRL* **2007**, *5*, 187.
[37] J. D. Poplawsky, N. R. Paudel, C. Li, C. M. Parish, D. Leonard, Y. Yan, S. J. Pennycook, *Adv. Energy Mater.* **2014**, *4*, 1400454.
[38] G. Stokkan, *J. Cryst. Growth* **2013**, *384*, 107.
[39] R. L. Woo, R. Xiao, Y. Kobayashi, L. Gao, N. Goel, M. K. Hudait, T. E. Mallouk, R. F. Hicks, *Nano Lett.* **2008**, *8*, 4664.
[40] E. Brown, C. Sheng, K. Shimamura, F. Shimojo, A. Nakano, *J. Appl. Phys.* **2015**, *117*, 054307.
[41] F. Bertolotti, L. Protesescu, M. V. Kovalenko, S. Yakunin, A. Cervellino, S. J. L. Billinge, M. W. Terban, J. S. Pedersen, N. Masciocchi, A. Guagliardi, *ACS Nano* **2017**, *11*, 3819.
[42] M. U. Rothmann, W. Li, Y. Zhu, U. Bach, L. Spiccia, J. Etheridge, Y.-B. Cheng, *Nat. Commun.* **2017**, *8*, 14547.
[43] S. Castellanos, K. E. Ekstrom, A. Autruffe, M. A. Jensen, A. E. Morishige, J. Hofstetter, P. Yen, B. Lai, G. Stokkan, C. del Canizo, T. Buonassisi, *IEEE J. Photovoltaics* **2016**, *6*, 632.
[44] D. P. Fenning, A. S. Zuschlag, J. Hofstetter, A. Frey, M. I. Bertoni, G. Hahn, T. Buonassisi, *IEEE J. Photovoltaics* **2014**, *4*, 866.
[45] M. I. Bertoni, S. Hudelson, B. K. Newman, D. P. Fenning, H. F. W. Dekkers, E. Carnagliotti, A. Zuschlag, G. Micard, G. Hahn, G. Coletti, B. Lai, T. Bounassisi, *Prog. Photovoltaics* **2010**, *19*, 187.
[46] Y. M. Yang, A. Yu, B. Hsu, W. C. Hsu, A. Yang, C. W. Lan, *Prog. Photovoltaics* **2015**, *23*, 340.
[47] A. Autruffe, V. Stenhjem Hagen, L. Arnberg, M. Di Sabatino, *J. Cryst. Growth* **2015**, *411*, 12.
[48] G. Stokkan, S. Riepe, O. Lohne, W. Warta, *J. Appl. Phys.* **2007**, *101*, 053515.
[49] I. Takahashi, N. Usami, H. Mizuseki, Y. Kawazoe, G. Stokkan, K. Nakajima, *J. Appl. Phys.* **2011**, *109*, 033504.
[50] D. W. deQuilettes, S. Jariwala, S. Burke, M. E. Ziffer, J. T.-W. Wang, H. J. Snaith, D. S. Ginger, *ACS Nano* **2017**, *11*, 11488.
[51] W. Tian, R. Cui, J. Leng, J. Liu, Y. Li, C. Zhao, J. Zhang, W. Deng, T. Lian, S. Ji, *Angew. Chem., Int. Ed.* **2016**, *55*, 13261.
[52] R. J. Stoddard, F. T. Eickemeyer, J. K. Katahara, H. W. Hillhouse, *J. Phys. Chem. Lett.* **2017**, *8*, 3289.
[53] L. W. Veldhuizen, G. W. P. Adhyaksa, M. Theelen, E. C. Garnett, R. E. I. Schropp, *Prog. Photovoltaics* **2017**, *25*, 605.
[54] D. Ritter, E. Zeldov, K. Weiser, *Appl. Phys. Lett.* **1986**, *49*, 791.
[55] I. Balberg, A. E. Delahoy, H. A. Weakliem, *Appl. Phys. Lett.* **1988**, *53*, 992.
[56] N. C. Halder, T. R. Williams, *Sol. Cells* **1983**, *8*, 201.
[57] J. Dugas, *Sol. Energy Mater. Sol. Cells* **1994**, *32*, 71.
[58] S. Banerjee, H. Saha, *Sol. Cells* **1990**, *28*, 77.
[59] A. B. Sproul, *J. Appl. Phys.* **1994**, *76*, 2851.
[60] G. E. Pike, C. H. Seager, *J. Appl. Phys.* **1979**, *50*, 3414.
[61] D. P. Joshi, D. P. Bhatt, *IEEE Trans. Electron Devices* **1990**, *37*, 237.
[62] R. Brendel, U. Rau, *J. Appl. Phys.* **1999**, *85*, 3634.
[63] S. M. Sze, K. K. Ng, *Physics of Semiconductor Devices*, John Wiley & Sons, Inc., Hoboken, NJ, USA **2007**.
[64] W. Shockley, *Electron and Holes in Semiconductors*, D. Van Nostrand Company, Inc., New York **1950**.
[65] Y. Yang, Y. Yan, M. Yang, S. Choi, K. Zhu, J. M. Luther, M. C. Beard, *Nat. Commun.* **2015**, *6*, 7961.
[66] B. G. Mendis, L. Bowen, Q. Z. Jiang, *Appl. Phys. Lett.* **2010**, *97*, 092112.
[67] J. Oualid, C. M. Singal, J. Dugas, J. P. Crest, H. Amzil, *J. Appl. Phys.* **1984**, *55*, 1195.
[68] H. C. Sio, S. P. Phang, D. Macdonald, *Solar RRL* **2017**, *1*, 1600014.
[69] M. Gloeckler, J. R. Sites, W. K. Metzger, *Appl. Phys. Lett.* **2005**, *98*, 113704.
[70] W. K. Metzger, I. L. Repins, M. Romero, P. Dippo, M. Contreras, R. Noufi, D. Levi, *Thin Solid Films* **2009**, *517*, 2360.
[71] R. Sheng, A. Ho-Baillie, S. Huang, S. Chen, X. Wen, X. Hao, M. A. Green, *J. Phys. Chem. C* **2015**, *7*, 3545.
[72] I. L. Braly, D. W. deQuilettes, L. M. Pazos-Outón, S. Burke, M. E. Ziffer, D. S. Ginger, H. W. Hillhouse, *Nat. Photonics* **2018**, *12*, 355.
[73] R. Brenes, D. Guo, A. Osherov, N. K. Noel, C. Eames, E. M. Hutter, S. K. Pathak, F. Niroui, R. H. Friend, M. S. Islam, H. J. Snaith, V. Bulović, T. J. Savenije, S. D. Stranks, *Joule* **2017**, *1*, 155.
[74] D. W. deQuilettes, S. Koch, S. Burke, R. K. Paranji, A. J. Shropshire, M. E. Ziffer, D. S. Ginger, *ACS Energy Lett.* **2016**, *1*, 438.
[75] Y. Yang, M. Yang, D. T. Moore, Y. Yan, E. M. Miller, K. Zhu, M. C. Beard, *Nat. Energy* **2017**, *2*, 16207.
[76] Y. Su, C. Liu, S. Brittman, J. Tang, A. Fu, N. Kornienko, Q. Kong, P. Yang, *Nat. Nanotechnol.* **2016**, *11*, 609.
[77] G. W. P. Adhyaksa, E. Johlin, E. C. Garnett, *Nano Lett.* **2017**, *17*, 5206.
[78] B. W. Silverman, *J. R. Stat. Soc.* **1982**, *31*, 93.
[79] J. M. Richter, M. Abdi-Jalebi, A. Sadhanala, M. Tabachnyk, J. P. H. Rivett, L. M. Pazos-Outón, K. C. Gödel, M. Price, F. Deschler, R. H. Friend, *Nat. Commun.* **2016**, *7*, 13941.
[80] Y. Yang, M. Yang, Z. Li, R. Crisp, K. Zhu, M. C. Beard, *J. Phys. Chem. Lett.* **2015**, *6*, 4688.